Measurements of Inclusive and Diffractive Electromagnetic Jet Transverse Single-Spin Asymmetry in Polarized p+p Collision at $\sqrt{s} = 200$ GeV at STAR

Latif Kabir, Xilin Liang[1]

October 20, 2022

[1]email: xilin.liang@email.ucr.edu

Contents

List of Figures

List of Tables

Chapter 1

Introduction

Transverse single-spin asymmetries (A_N), which are defined as left-right asymmetries of the particle production with respect to the plane defined by the momentum and spin directions of the polarized beam, have been observed to be large for charged- and neutral-hadron production in hadron-hadron collisions over a couple of decades [1, 2, 3, 4, 5]. In pQCD, however, the A_N is predicted to be small and close to zero in high energy collisions [6]. There are two major frameworks that can provide a potential explanation for such sizeable asymmetries. The first one is the transverse-momentum-dependent (TMD) contributions from the initial-state quark and gluon Sivers functions and/or the final-state Collins fragmentation functions. In the Sivers mechanism, the asymmetry comes from the correlation between the proton spin and the parton transverse momentum [7], while the Collins effect arises from the correlation between the spin of the fragmenting quark and the outgoing hadron's transverse momentum [8]. Another framework is based on the twist-3 contributions in the collinear factorization framework, including the quark-gluon or gluon-gluon correlations and fragmentation functions [9].

According to the study by CMS Collaboration [11], diffractive interactions contribute to about a significant fraction ($\sim$ 25%) of the total inelastic p+p cross section at high energies. The simulation for hard diffractive events based on PYTHIA-8 predicts that the fraction of diffractive cross section in the total inclusive cross section at the forward region is about 20% [4]. In recent years, analyses of A_N for forward π^0 and electromagnetic jets (EM-jets) in $p^{\uparrow} + p$ collisions at STAR indicated that there might be non-trivial contributions to the large A_N from diffractive processes [5, 10]. Measuring the A_N of diffractive process will provide an opportunity to study the properties and understand the diffractive exchange in p+p collisions.

The analyses consist of two parts: inclusive EM-jet A_N at run 15 FMS

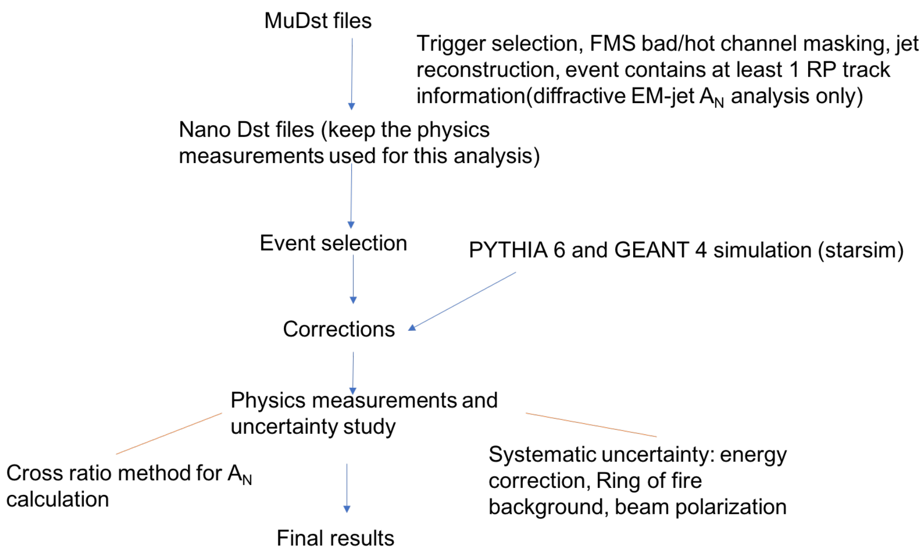

Figure 1.1: General analysis procedures for inclusive and diffractive EM-jet A_N analyses

and diffractive EM-jet A_N at run 15 FMS. Compared to the previously STAR published paper [5], the former analysis on focuses on inclusive EM-jet A_N for the dependence on photon multiplicity inside the EM-jet, EM-jet transverse momentum (p_T) and energy. The later analysis is the first measurement for diffractive EM-jet A_N at STAR.

The structure of the analysis note follows the analysis procedures in Fig.(1.1). Chapter 2 will present the dataset and the data quality assurance (QA). Chapter 3 will present the event selection. Chapter 4 will present the corrections. Chapter 5 will present the systematic uncertainty. Chapter 6 will present the final results.

Chapter 2

Dataset and Quality Assurance (QA)

2.1 General information for the dataset

The inclusive and diffractive EM-jet A_N analyses both utilize polarized p+p collision at $\sqrt{s} = 200$ GeV taken in run 15. Details of the data set are listed as follow:

- Trigger setup name: production_pp200trans_2015
- Data stream: fms
- Production tag: P15ik
- File type: MuDst files in Distributed Disk (DD)

The run list for the analyses is in Appendix (A).

Both analyses generate smaller size data stream files (DST) from the MuDst files, applying trigger filter (described in Sec. (2.2)) and jet reconstruction (described in Sec. 2.4). In addition, the events with at least one Roman Pot track are required for diffractive EM-jet A_N analysis when generating the DST files.

2.2 Triggers

9 triggers for FMS are used for both analyses. The triggers with their ID are listed in Table (2.1). However, the FMS-sm-bs2 trigger is considered as a source of background and excluded from the trigger list in the final results. Details can be seen in 5.2.1.

Table 2.1: Trigger name lists and trigger ID for run 15

Trigger name	Trigger ID
FMS-JP0	480810 / 480830
FMS-JP1	480809 / 480829
FMS-JP2	480808 / 480828
FMS-sm-bs0	480801 / 480821 / 480841
FMS-sm-bs1	480802 / 480822
FMS-sm-bs2	480803 / 480823 / 480843
FMS-lg-bs0	480804 / 480824 / 480844
FMS-lg-bs1	480805 / 480825
FMS-lg-bs2	480806 / 480826

The run-by-run QA for trigger distribution is checked. Figure (xxx) shows the XXX trigger distribution for all the runs for inclusive processes as example. The other trigger distributions are shown in Appendix (B).

2.3 Calibration

The calibration for run 15 FMS dataset are from STAR framework [14], but with some additional steps. They mainly include the following items:

- Bit shift (BS): It refers to the binary bit, used to store the ADC value, not starting from the normal lowest bit. The BS will affect a cell's ADC distribution and the corresponding hit energy. The approach to check the BS is to use the ADC of each FMS hit to check with its corresponding BS value of the cell [15].

- Gain and gain correction: The energy of the hit = ADC $\times$ gain $\times$ gain correction. The gain is the calculated value based on a cell's η position, while the gain correction is obtained from offline calibration [14]. The flag of the gain and the gain correction for each tower in the STAR database is "fmsGainCorr-BNL-C".

- Hot channel and bad channel masking: A hot channel refers to the tower with a number of hits far more than the average number of hits for the whole detector towers within some time range. A bad channel refers to the

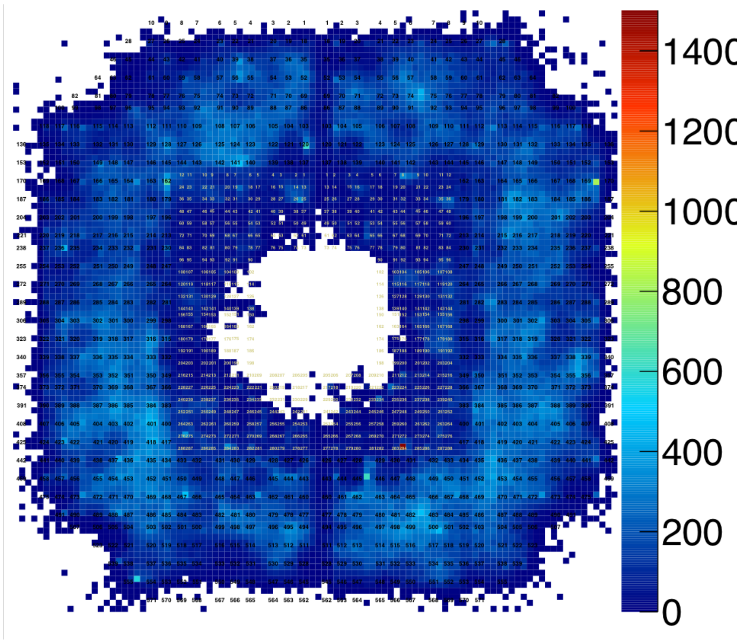

Figure 2.1: Example of EM-jet distribution at FMS before additional hot channel masking. The red color area in this plot indicates the possible hot channels.

problematic towers which might be suffered from hardware issues. Both hot channels and bad channels can affect the quality of the calibration and the analyses since there are quite a lot of not physical signals contaminated. To mask out these channels, the gain values are set to zero. In addition to the existing hot channel and bad channel masking from STAR calibration [14], the fill-by-fill hot channel masking is applied in both analyses. The EM-jet distribution before any event selections for every fill is checked to find out any possible hot channels. The EM-jet reconstruction is discussed in 2.4. Figure (2.1) shows one example of the EM-jet distribution at the FMS. The areas with extremely high EM-jet entries compared to the overall average entries in the plot are assumed to be the hot channel area. The channels within these areas are considered hot channels and added manually to the hot channel lists. Figure (2.2) shows the EM-jet distribution for fill 18827 as an example after the additional hot channel masking. From the plot, the hot channels disappear and the entries of the majority of towers are close to the average entries.

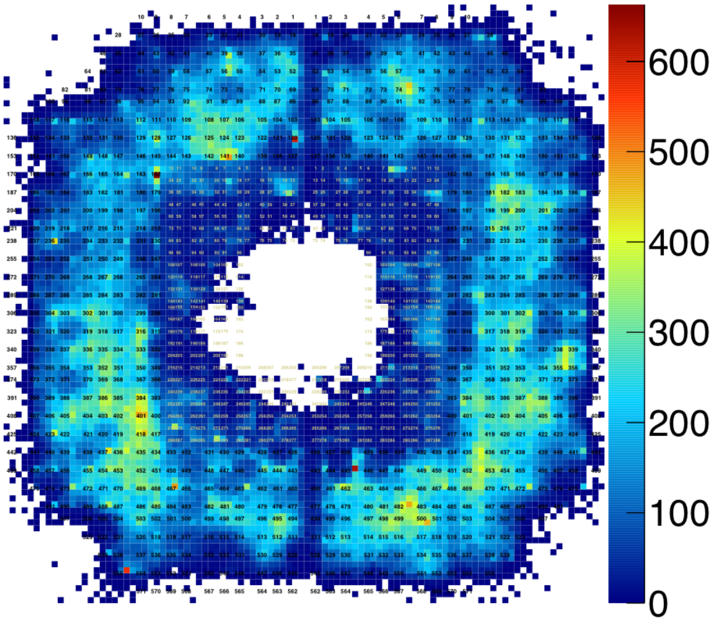

Figure 2.2: Example of EM-jet distribution at FMS after additional hot channel masking.

2.4 Electromagnetic jet reconstruction

The Electromagnetic jets (EM-jets) are the jet consisting of only photon. The photon candidates for EM-jets reconstruction are the FMS points. The FMS points are formed by the shower shape fitting for the FMS clusters, where the FMS clusters are the groups of adjacent FMS hits by FMS cluster finding algorithm. The hits are the basic reconstructed object in the FMS, which are formed by the towers with non-zero ADC value [12].

In order to reduce the noise background, the FMS points with $E > 2GeV$ and $E_T > 0.2GeV$ are considered in the analysis. The EM-jets are reconstructed with the anti-k_T algorithm from the FastJet package [13], with the resolution parameter $R = 0.7$. The primary vertex of the EM-jets are determined according to the priority of TPC vertex, BBC vertex and VPD vertex. If the primary vertex is unable to determined among these three detectors, it will set to be (0,0,0).

Figure (xxx) shows the EM-jet kinematic for the inclusive process.

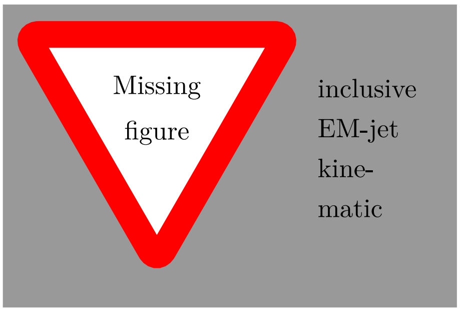
Missing
figure
inclusive
EM-jet
kine-
matic

Chapter 3

Event Selection

The event selections for inclusive and diffractive EM-jets include the following items:

1. Triggers: The triggers used for both analyses are the FMS BS triggers and FMS JP triggers. They are listed in Table(2.1). Only the events with any triggers fired are kept.

2. EM-jet reconstruction: EM-jets are reconstructed by FMS point by Anti-k_T algorithm with R = 0.7. The FMS points are required to have $E > 2$ GeV and $E_T > 0.2$ GeV. Details of the EM-jet reconstruction are in Section (2.4)

3. EM-jet cut: Details of the EM-jet cuts are in Section (3.1)
    - The EM-jets for inclusive EM-jet analysis are required to have $p_T > 2$ GeV, while the EM-jets for diffractive EM-jet analysis are required to have $p_T > 1$ GeV.
    - The vertex z are within [-80, 80] cm.
    - The pseudorapidity (η) of the EM-jets are within [2.8, 3.8] for inclusive EM-jet analysis and [2.6, 4.1] for diffractive EM-jet analysis.
    - The event with EM-jet $|x_F| > 1$ or $E > 100$ GeV are excluded.
    - The number of EM-jets for each event is not zero.

4. Event property cut: Details of the event property cuts are in Section (3.2)
    - Veto on abort gap.
    - The spin status for the blue beam and yellow beam is correct and accept the 4 cases of 4-bit spin patterns.

5. Roman Pot (RP) track cut: These cuts are only used for diffractive EM-jet analysis. Details are in Section (3.3)

    - Only accept the event with the following 2 cases: no east side RP track and only one west side RP track; only one east side RP track and only one west side RP track.
    - Each RP track must hit at least 7 RP silicon planes.
    - Each RP track must satisfy $-2 < \theta_x < 2$ mrad and $1.5 < |\theta_y| < 4.5$ mrad.

6. Background cut: Details of the background cut are in Section (3.4).

    - Ring of fire cut (for both analyses): Exclude FMS-sm-bs3 trigger.
    - sum energy cut (only for diffractive EM-jet analysis): Cut on the sum of west side RP track energy and EM-jet energy. Details in Table (???).
    - West BBC ADC sum cut (only for diffractive EM-jet analysis): west side large BBC ADC sum < 80 and west side small BBC ADC sum < 100.

7. Corrections: Apply EM-jet energy correction (details in Sector(???)) and Underlying-Event (UE) correction (details in Sector(???))

3.1 EM-jet cut

The EM-jet reconstruction is based on the anti-k_T algorithm by the FastJet package, with the R parameter 0.7, which is described in 2.4. To reduce the background EM-jet, the p_T cut is applied. For the inclusive EM-jet, the cut is $p_T < 2$ GeV. However, the diffractive process applies the cut on EM-jet $p_T < 1$ GeV, due to the limited statistics for this process.

The EM-jet vertex is determined by the primary vertex following the priority of TPC, BBC ,and VPD. If the primary vertex can be obtained by TPC, the TPC vertex will be the primary vertex. Otherwise, check the BBC vertex on the next step. If there is no BBC vertex, then check the VPD vertex. If there is still no VPD vertex, the primary vertex is set to be z=0. The vertex z cut on $|z| < 80$ cm is considered for both inclusive and diffractive processes.

In addition, we apply the cut on EM-jet η which aims to get rid of the bad reconstructed EM-jets and the EM-jets hitting outside the FMS. Therefore, the EM-jet cut are [2.8, 3.8] for inclusive EM-jet analysis and [2.6, 4.1] for diffractive EM-jet analysis.

Table 3.1: 4 acceptable 4-bit spin patterns

4-bit spin	Translate	Blue beam polarization	Yellow beam polarization
0101	5	up	up
0110	6	up	down
1001	9	down	up
1010	10	down	down

Also, the events with EM-jet energy $E > 100$ GeV or $|x_F| > 1$ are discarded, where Feynman-x x_F can be estimated by the EM-jet energy divided by the beam energy ($x_F = \frac{2E}{\sqrt{s}}$). Those events are possibly pile-up events.

Finally, the events are required to have non-zero EM-jets. Although those events with zero EM-jets are not counted in the EM-jet yield when calculating the A_N, they still have effects in polarization calculation, which have some effects on the final A_N results. Applying the non-zero EM-jet cuts will solve this issue and calculate the precise polarization.

3.2 Event property cut

The abort gap for both blue beam and yellow beam is within bunch ID [31, 39] and [111, 119] for run 15. Figure (3.1) shows one example of bunch crossing distribution for one physics run. The bunches with low entries are the abort gap. The events with either blue beam or yellow beam with the abort gap are discarded.

The spin patterns for each beam, either up or down, are obtained from the bunch crossing of each event. The translation from the database for the spin patterns is described in [16]. The spin patterns for both blue and yellow beam are combined as 4-spin bit. The events satisfying the following 4 4-spin bit cases in Table (3.1) are considered in both analyses. These patterns require the polarization of both blue and yellow beam either up or down.

3.3 Roman Pot track cut

Roman Pot (RP) detector is used for detecting the slightly scattered proton along the beam. The RP tracks are generally recognized as slightly scattered protons. To identify the diffractive process, the coincidence between the FMS detector and RP detector is required, which can satisfy the requirement of the presence of the rapidity gap for the diffractive process. Therefore, two possible channels are considered for the diffractive processes, which can be shown in Figure (3.2). Figure (3.2 top) shows the diffractive channel requiring no east

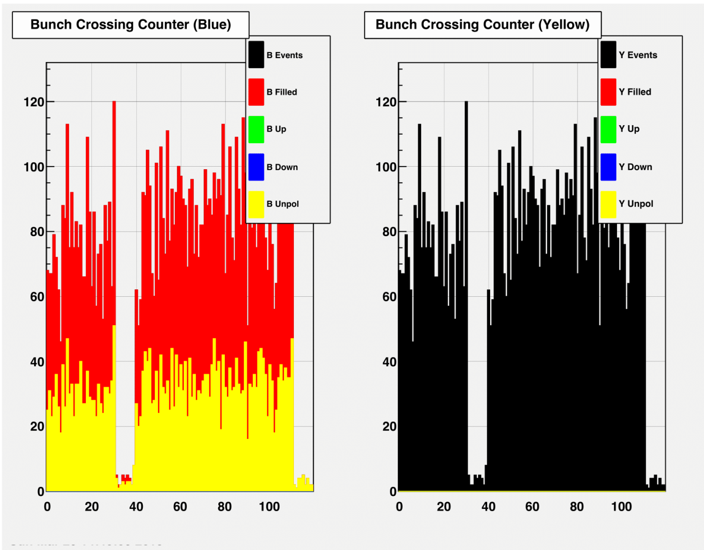

Figure 3.1: Bunch crossing distribution for run 16088023 as example. Left plot shows the blue beam bunch crossing distribution; right plot shows the yellow beam bunch crossing distribution. The abort gap for both blue beam and yellow beam are with bunch ID [31, 39] and [111, 119].

side RP track and only one west side RP track, while Figure (3.2 bottom) shows another channel requiring only one east side RP track and only one west side RP track. Channels other than the 2 acceptable cases are not considered because they might contain background noise or pile-up events.

The next step is to identify if the RP tracks are good tracks. First of all, the RP track needs to hit at least 7 silicon planes. According to the RP design, there are 2 sets of RP (inner and outer) on each side. Each set contains a package above and below the beamline. Each package contains 4 silicon planes, where 2 of them are used to determine the hit position in x direction and the rest 2 are used to determine the hit position in y position direction. The requirement of RP track hitting at least 7 silicon planes will make sure not only the RP track hits both packages, but also the hit position and track momentum can be reconstructed more precisely. In addition, this cut can reduce the RP tracks from background noise significantly, since a large number of background tracks hit less than 4 silicon planes.

Then, the cuts on the polar angle of the RP tracks in the x-z plane (θ_x) and y-z plane (θ_y) are applied to make sure the RP tracks are good reconstructed tracks. The ranges of the cuts are obtained from the RP track θ_x and θ_y distribution in both simulation and data. The simulation is based on RP, using the Pythia8 + GEANT4 simulation framework. The details of the RP simulation and the description of the cuts from the simulation are in Appendix (C). Figure (3.3) show the only east side RP track θ_x (left plot) and θ_y (right plot) for data with the cut on the number of silicon planes that RP track hit, and Figure (3.4) show the only west side RP track θ_x (left plot) and θ_y (right plot) for data with the cut on the number of silicon planes that RP track hit.

3.4 Background cut

There are quite a large number of pile-up events in data, which have a serious impact on measuring the diffractive EM-jet A_N precisely. To deal with this effect, two additional sets of cuts are applied to minimize the pile-up effect.

The first set of cuts is based on the sum of west side RP track energy and EM-jet energy (sum energy). As shown in Figure (3.2), both possible channels contain only one west side RP track and EM-jets at FMS. In addition, the accidental coincident events usually have the sum energy greater than the proton beam energy, so it's a good idea to consider the cut based on the sum energy. The cuts on the sum energy are varied by the different x_F regions, where x_F is the scaling variable of the particle in the hadronic collision and can be calculated as the EM-jet energy divided by the proton beam energy for the FMS EM-jets. The cuts are based on the splitting of the two peaks for

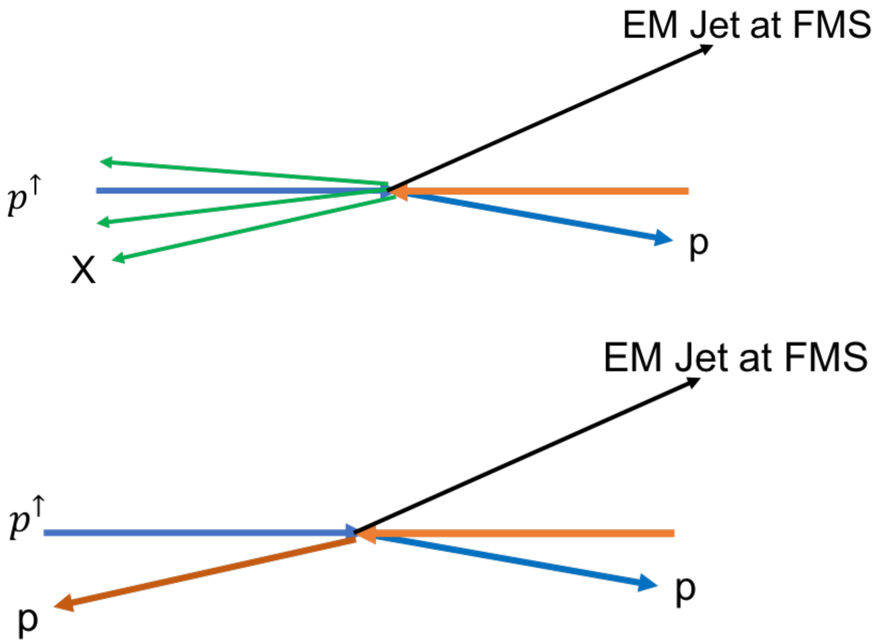

Figure 3.2: 2 possible channels for diffractive processes.

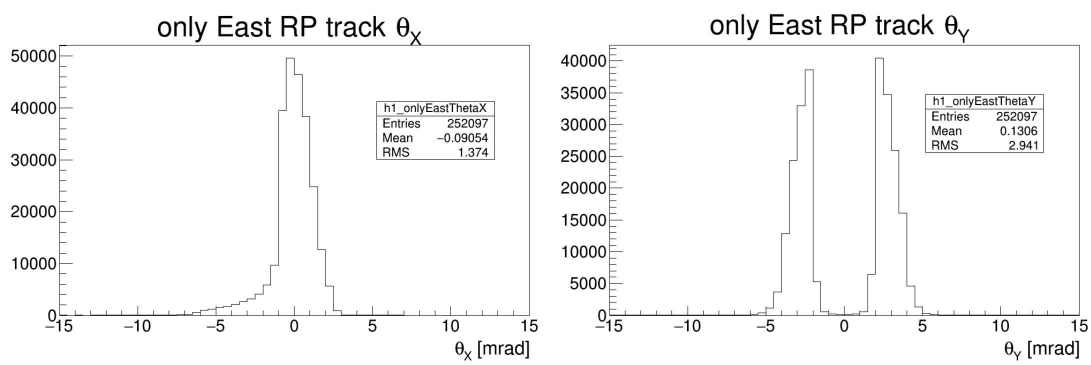

Figure 3.3: Distribution of the east side RP track θ_x (left plot) and θ_y (right plot)

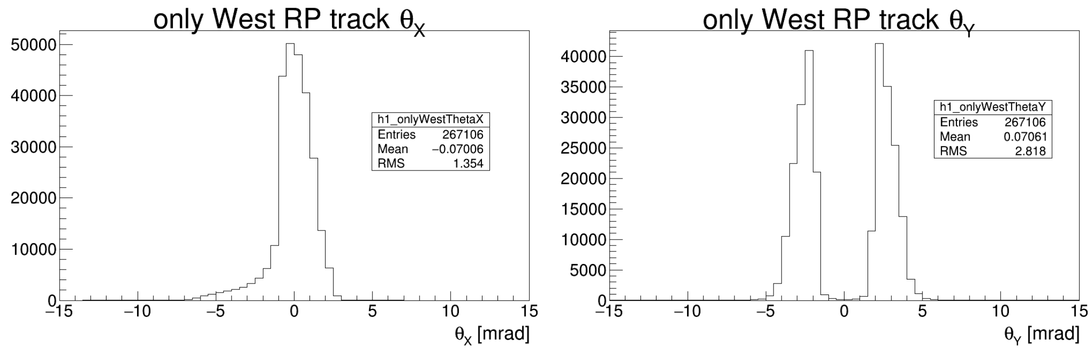

Figure 3.4: Distribution of the west side RP track θ_x (left plot) and θ_y (right plot)

Table 3.2: Sum energy cut for different x_F bins

x_F	Sum energy [GeV]
[0.1, 0.15]	<108
[0.15, 0.2]	<108
[0.2, 0.25]	<110
[0.25, 0.3]	<110
[0.3, 0.45]	<115

each sum energy distribution (Figure (3.5)), where the peak with the lower sum energy (close to beam energy, 100 GeV) is considered as the contribution from the diffractive processes and the peak with the higher sum energy is considered as the contribution from the pile-up events. Table (3.2) shows the sum energy cuts for the EM-jets at each xF region.

The second cuts are based on the Beam-Beam Counter (BBC), which is used for triggering, luminosity monitoring and local polarization measurement [?]. Generally, the pile-up events are more likely to appear in the high luminosity collision. In addition, the higher luminosity detected in an event, the higher the BBC ADC sum value will be collected. To decide the threshold of the BBC ADC sum value from the event, the combination with sum energy cut is considered to determine these cuts from BBC. In this analysis, only the west side BBC detector responses are considered. Based on the BBC design, the BBC ADC sum values from 2 different regions (small BBC and large BBC) are considered. Figure (3.6) show the 2-dimension distribution of sum energy and west side small (large) BBC ADC sum. To simplify, the events with sum energy less than 108 GeV are considered signals while the events with sum energy greater than 108 GeV are considered backgrounds. Also, to better qualify the cuts, the ratios of signals to backgrounds by every BBC ADC sum bin are calculated and

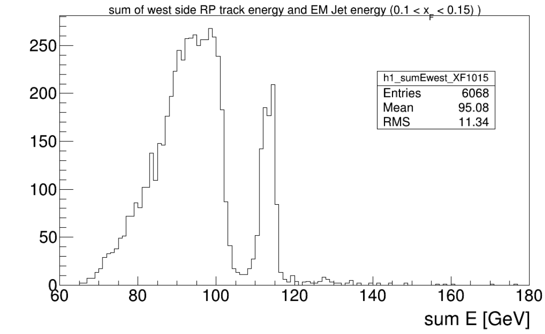

(a) Sum energy distribution for EM-jet with $0.1 < x_F < 0.15$.

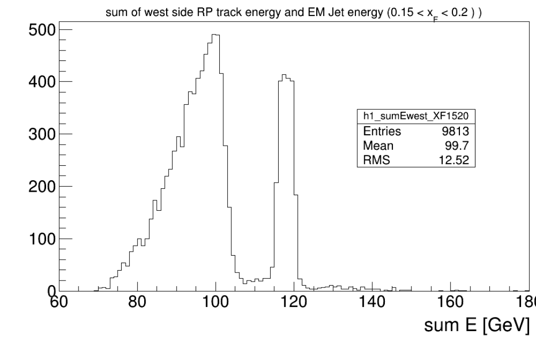

(b) Sum energy distribution for EM-jet with $0.15 < x_F < 0.2$.

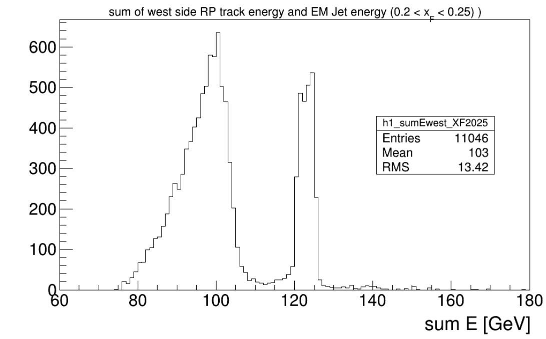

(c) Sum energy distribution for EM-jet with $0.2 < x_F < 0.25$.

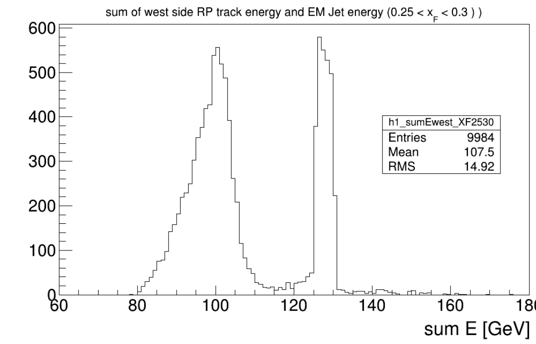

(d) Sum energy distribution for EM-jet with $0.25 < x_F < 0.3$.

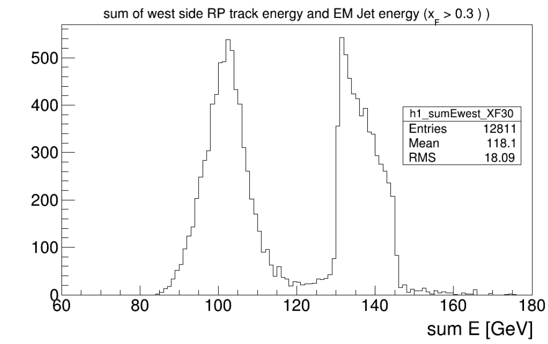

(e) Sum energy distribution for EM-jet with $0.3 < x_F < 0.45$.

Figure 3.5: Sum energy distribution for EM-jet with $0.1 < x_F < 0.45$, but separate by 5 different x_F region.

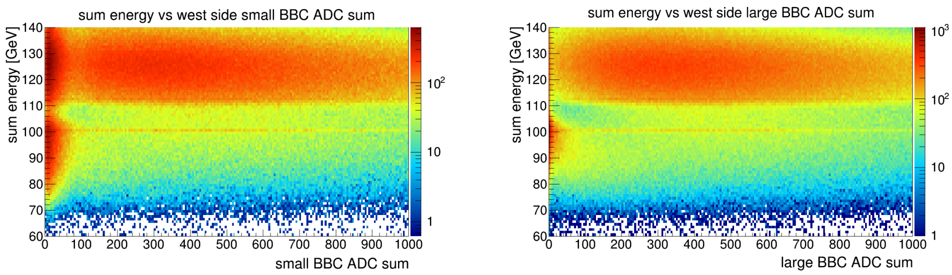

Figure 3.6: Distribution of sum energy vs west side small BBC ADC sum (left plot) and sum energy vs west side large BBC ADC sum (right plot). The region with sum energy > 108 GeV is considered as background and the region with sum energy < 108 GeV is considered as signal.

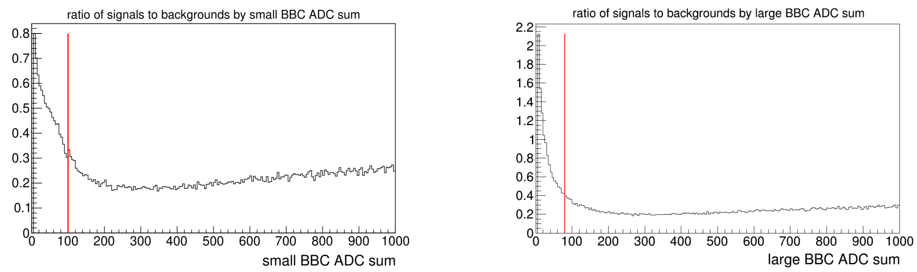

Figure 3.7: Distribution of signals to backgrounds by every small BBC ADC sum bin (left) and by every large BBC ADC sum bin (right). The red vertical line indicate the proper cut for small (large) BBC ADC sum.

presented in Figure (3.7). From the figures, the west side small BBC ADC sum cut is less than 100 and the west side large BBC ADC sum cut is less than 80.

Chapter 4

Corrections

4.1 Underlying Event (UE) correction

4.1.1 Underlying Event energy correction for diffractive process

The underlying event is a part of a jet, not from the parton fragmentation but from secondary scattering or other processes. This will deposit some energy to the jet, so the correction on UE is required to subtract its energy (momentum) from the jet. The commonly used method is the "cross-ratio" method [19]. In this method, first of all, two off axis jets with same pseudorapidity but at $\pm 1/2\pi$ azimuthal angle at the edge of the original jet are reconstructed as UE background. Then, the UE energy density can be calculated using $\rho = E/(\pi R^2)$, where E is the UE energy and R is the UE jet radius. The fastjet program use the "ghost particle" technique to calculate the UE energy density (ρ) and jet area (A). The maximum "ghost particle" η is 5.0 and the "ghost area" is 0.04. Finally, the jet energy will be subtracted by the UE energy: $E_{corrected} = E_{original} - \rho \times A$, where the corrected EM-jet energy is $E_{corrected}$ and the original EM-jet energy is $E_{original}$.

Figure (4.1) show the UE correction distribution for EM-jet energy. The left plot shows the subtraction term for the UE correction for EM-jet energy. The right plot shows the EM-jet energy distribution after the UE correction. If the EM-jet energy after subtraction is less than 0 GeV, the energy will be set to 0 GeV.

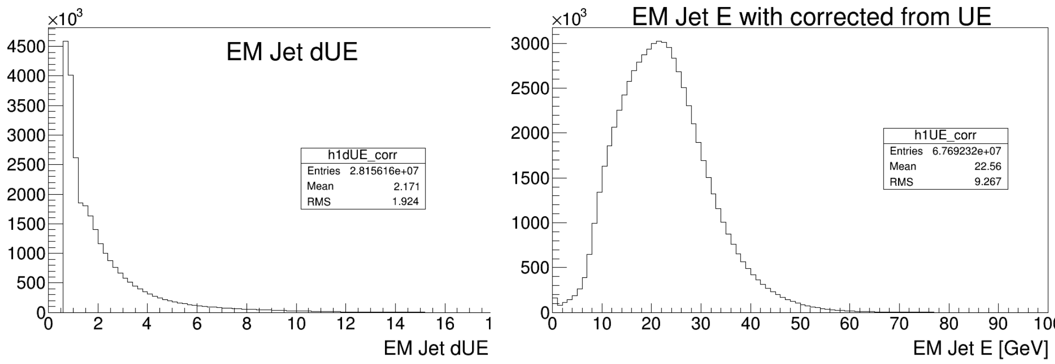

Figure 4.1: UE distribution for diffractive EM-jet analysis. The left plot shows the subtraction term $\rho \times A$. The right plot shows the EM-jet energy distribution after the UE correction.

4.1.2 Underlying Event energy correction for inclusive process

The UE correction for the inclusive process is similar to that for the diffractive process, but the correction object is the EM-jet transverse momentum instead of energy. The UE correction method, setup and procedures are the same as explained in Sec. (4.1.1). Since the correction object is the p_T, the calculation formula for EM-jet with UE correction is $p_{T,corrected} = p_{T,original} - \rho \times A$, where the corrected EM-jet p_T is $p_{T,corrected}$, the original EM-jet p_T is $p_{T,original}$, UE p_T density is ρ and jet area is A, respectively.

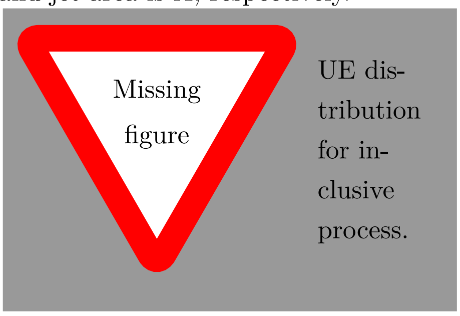

4.2 Detector level to particle level EM-jet energy correction

The EM-jet energy obtained from FMS is considered detector level EM-jet energy. Therefore, a correction for detector level to particle level EM-jet energy is necessary for both analyses. The correction is based on the Monte Carlo simulation for FMS. The details of the simulation are shown in (D). In the simulation,

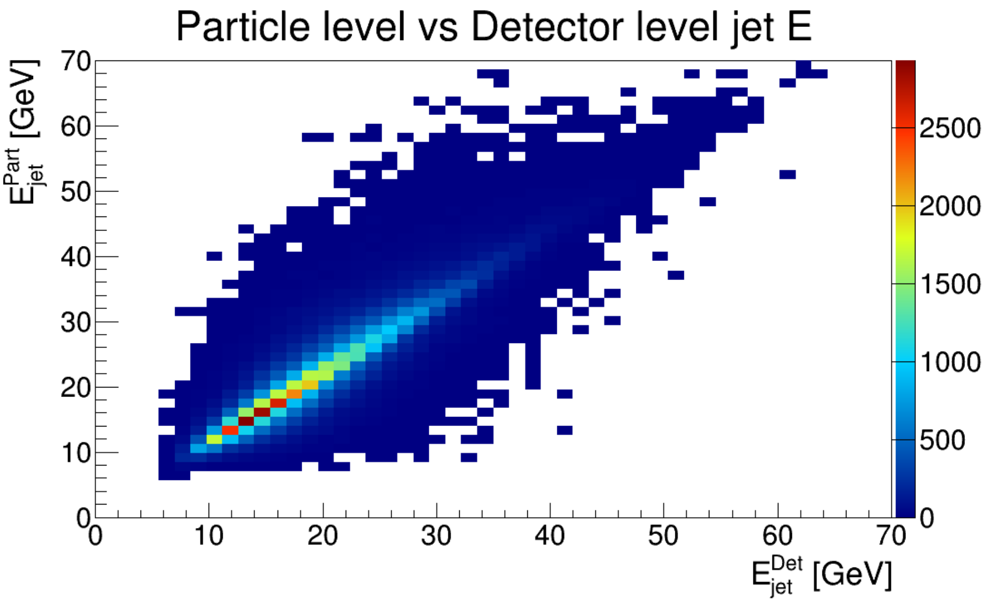

Figure 4.2: EM-jet energy distribution in particle level (y axis) and detector level (x axis) from the FMS simulation.

the EM-jets with both particle level and detector level are recorded. Figure (4.2) shows the EM-jet energy distribution in particle level (y axis) and detector level (x axis). Figure (4.3) shows the profile of the EM-jet energy distribution with particle level and detector level. The black points are the correlation between the EM-jet energy in particle level and detector level. The red curves are the fit for the points in two different detector level regions: $5 < E < 10$ GeV and $10 < E < 60$ GeV. The 6th-order polynomial function is used for fitting the former region and the linear function is used for fitting the latter region. These functions are used to calculate the corrected energy from the original detector level energy. The corrected EM-jet energy will finally applied for the x_F calculation and A_N extraction.

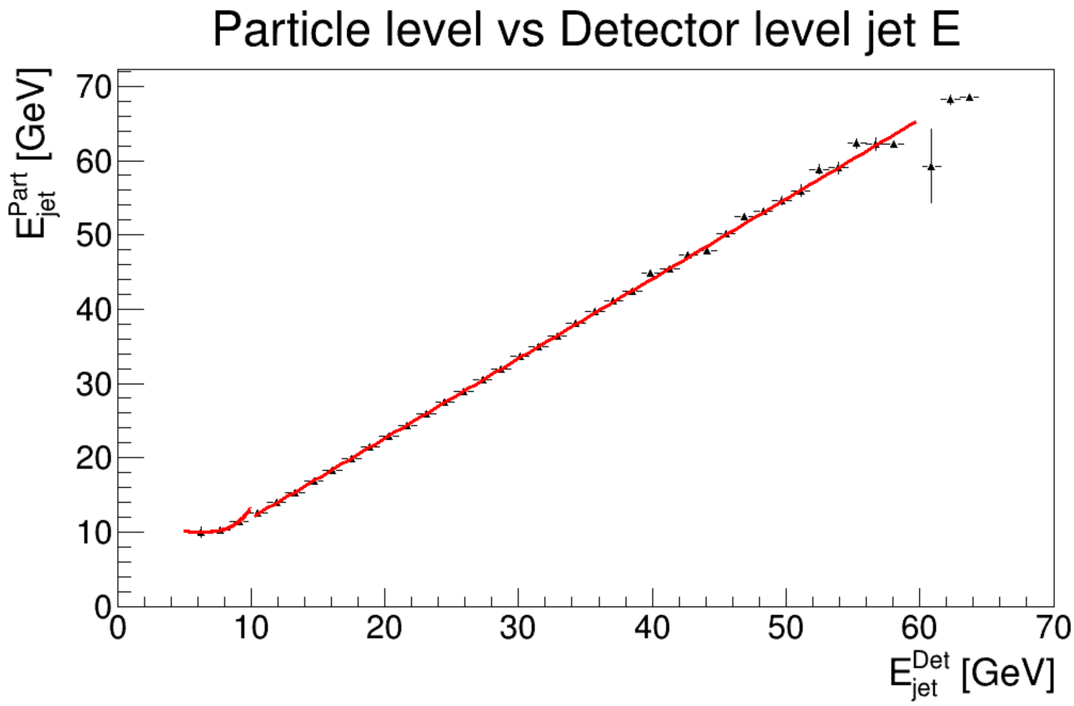

Figure 4.3: The profile of the EM-jet energy distribution with particle level and detector level. The black points are the correlation between the EM-jet energy in particle level and detector level. The red curves are the fit for the black points.

Chapter 5

Systematic Uncertainty

5.1 Energy Uncertainty

The systematic uncertainties of EM-jet energy consist of three parts: calibration uncertainty, radiation damage uncertainty, and energy resolution and correction uncertainty.

5.1.1 Calibration uncertainty

The calibration of FMS towers is done by π^0 reconstruction, which is from two photons reconstruction. The gain correction of each tower is calculated and corrected based on the extraction of the invariant mass peak of the two photons. In this way, the gain correction for all the towers can be correlated. However, the invariant mass peak extraction is biased, based on the fit functions for the signal peak and the background. Therefore, the biased invariant mass peak will raise the uncertainty for the gain correction calculated, which can finally affect the accuracy of the energy of the towers.

To estimate such uncertainty, the invariant mass mean difference extracted from two different cases of fitting for the 2-photon invariant mass distribution can be assigned as the energy uncertainty. This uncertainty is estimated to be about 2.5% [12].

5.1.2 Radiation Damage Uncertainty

The radiation damage is already a common issue for the FMS detector. This damage will introduce systematic uncertainty for the energy in FMS. For the FMS, there is a LED system which can monitor and qualify the radiation damage by observing the long-term gain change for the FMS towers. This gain change

x_F	Energy uncertainty
0.125	8.78%
0.175	3.24%
0.225	3.79%
0.275	4.09%
0.325	4.74%

Table 5.1: Energy correction systematic uncertainty for diffractive EM-jet analysis, separating by each x_F region.

information can be used to estimate the contribution of systematic uncertainty by the radiation damage [12].

A study had been done to parameterize the radiation damage for run 15 FMS [21]. This study shows the systematic uncertainty for run 15 FMS due to the radiation damage is less than 0.5%.

5.1.3 Energy Correction Uncertainty

Detector level EM-jet energy to particle level EM-jet energy correction has been done. Since this correction is calculated by the polynomial functions, we assign the systematic uncertainty by changing the polynomial functions to express this correction. For the EM-jet energy ranging [5, 10] GeV, the 5-th order polynomial function is applied to calculate the energy correction for systematic uncertainty study. Similarly, the 2-nd order polynomial function is applied for EM-jet energy ranging [10, 60] GeV. Then the energy resolution is calculated using Equation (5.1), where the $E_{systematic}$ is the energy correction calculated using the function for systematic uncertainty study, and the $Eoriginal$ is the energy correction calculated using the function explained in Sec. (4.2). The maximum energy resolution for each x_F region is regarded as the systematic uncertainty for the energy correction.

$$energy\,resolution = \frac{|E_{systematic} - E_{original}|}{E_{original}} \tag{5.1}$$

For the diffractive EM-jet analysis, the energy systematic uncertainty is listed in Table (5.1), which includes the calibration uncertainty, radiation damage uncertainty, and energy correction uncertainty.

x_F	E_{sum} cut original	E_{sum} cut for systematic uncertainty
0.1 - 0.15	E_{sum} <108 GeV	E_{sum} <112 GeV
0.15 - 0.2	E_{sum} <108 GeV	E_{sum} <112 GeV
0.2 - 0.25	E_{sum} <110 GeV	E_{sum} <114 GeV
0.25 - 0.3	E_{sum} <110 GeV	E_{sum} <114 GeV
0.3 – 0.45	E_{sum} <115 GeV	E_{sum} <120 GeV

Table 5.2: Sum energy cut for original study and systematic uncertainty study.

5.2 Background uncertainty

The background uncertainty contributes to the systematic uncertainty of the final results of A_N. For the inclusive EM-jet analysis, the background uncertainty includes the uncertainties on pile-up, abort gap, Ring of Fire, Underlying events, and Unfolding. For the diffractive EM-jet analysis, the background uncertainty includes the uncertainties on Ring of Fire, sum energy cuts, and BBC cuts.

5.2.1 Ring of Fire uncertainty

The Ring of Fire uncertainty is applied for both analyses. This background is related to the FMS-sm-bs3 trigger. This trigger is targeted at the inner region of FMS which is close to the beam. It's generally recognized that the beam remnants are accepted by FMS-sm-bs3 trigger. Therefore, this trigger is filtered out in both analyses and considered as a source of background. The A_N result difference between considering this trigger and excluding this trigger will be the systematic uncertainty for this background.

5.2.2 Sum energy cut uncertainty

The sum energy cut uncertainty is applied only for diffractive EM-jet analysis. Details of the sum energy cut are in Sec. (3.4). The sum energy cuts are slightly changed, and the A_N result difference before and after such changes are calculated as the sum energy cut uncertainty. The changes of sum energy cut for systematic uncertainty study are listed in Table (5.2).

5.2.3 BBC cut uncertainty

The BBC cut uncertainty is only applied for diffractive EM-jet analysis. The details of the BBC cuts are shown in Sec. (3.4). There are slightly changes for the cuts on west side large (small) BBC ADC sum in order to study for the systematic uncertainty. For the large BBC ADC sum cut, the cut change from

$\|x_F\|$	Ring of Fire	E_{sum}	Small BBC	Large BBC	Summary
0.125	4%	30%	21%	26%	45%
0.175	22%	10%	7%	12%	28%
0.225	16%	4%	14%	7%	23%
0.275	22%	6%	1%	10%	25%
0.325	4%	0%	1%	5%	6%

Table 5.3: Background systematic uncertainty for diffractive EM-jet A_N result of blue beam ($x_F > 0$)

$\|x_F\|$	Ring of Fire	E_{sum}	Small BBC	Large BBC	Summary
0.125	15%	59%	4%	46%	77%
0.175	4%	7%	10%	16%	21%
0.225	2%	14%	11%	28%	34%
0.275	9%	53%	6%	76%	93%
0.325	17%	7%	5%	5%	20%

Table 5.4: Background systematic uncertainty for diffractive EM-jet A_N result of yellow beam ($x_F < 0$)

60 to 65. For the small BBC ADC sum cut, the cut change from 100 to 105. The two changes are applied separately to study the systematic uncertainty by calculating the difference for the A_N results with and without the changes.

5.2.4 Summary for the background uncertainty

Table (5.3) (Table (5.4)) shows the background uncertainty for each individual term and the summary term for blue (yellow) beam A_N for diffractive EM-jet A_N results. The summary term use the sum of the square for each individual term: $\sigma = \sum_i \sigma_i^2$.

5.3 Polarization uncertainty

The blue beam and yellow beam polarization is used to calculate the A_N results. As a habit, the uncertainty of beam polarization uncertainty is listed independently. The beam polarization measurement results are provided by the CNI group, which develops, maintains and operates the RHIC polarimeter measurement. The beam polarization measurement results are listed in the table in webpage [22]. In the webpage, the starting time (t_0), the polarization of the blue (yellow) beam at the beginning of every fill (P_0), the decay rate ($\frac{dP}{dt}$) are provided for each fill. For each event, the beam polarization can be calculated from the time difference from the beginning of the fill using Equ. (5.2), where

t_{event} is the time of each event. The beam polarization for each run can be calculated by Equ. (5.3), where t_{run} is the time of the center of the run. The beam polarization for each fill can be calculated with the weighted average run polarization with Equ. (5.4), where L_{run} is the luminosity of each run. However, since L_{run} is proportional to the number of events in each run, the number of events in each run can replace the luminosity of each run in the calculation.

$$P_{event} = P_0 + \frac{dP}{dt}(t_{event} - t_0) \tag{5.2}$$

$$P_{run} = P_0 + \frac{dP}{dt}(t_{run} - t_0) \tag{5.3}$$

$$P_{fill} = \frac{\sum_{run} L_{run} P_{run}}{\sum_{run} L_{run}} \tag{5.4}$$

The uncertainty of beam polarization includes three parts: the scale uncertainty, fill-to-fill uncertainty, and uncertainty from the profile correction procedure [23].

The scale uncertainty is related to the polarization measurement methods. It includes H-jet scale, H-jet background and pC scale. For run 15, the scale uncertainty is 3% [23].

The relative uncertainty of the profiles correction for one beam in one fill is 2.2%. For a set of M fills, the relative profile correction for the single-spin asymmetry measurement is $\sigma(profile)/P = 2.2\%/\sqrt{M}$ [23]. For the run 15 FMS dataset used for both analyses, this uncertainty is about 0.3%.

The fill-to-fill uncertainty is propagated based on Equ. (5.4) with the uncertainty of P_0 and $\frac{dP}{dt}$. The uncertainty for these two terms $(\sigma(P_0))$ and $(\sigma(\frac{dP}{dt}))$ for either blue beam or yellow beam can be obtained in [22]. This uncertainty can be expressed in Equ. (5.5). The third term on the right side of the equation is due to the sensitivity of the measurement of the energy scale of the nuclei in the pC polarimetry [12], and it's negligible. However, for the term (Equ. (5.6)), this correction is overcounting for the measurement using a fraction of the run period. Therefore, a correction scale factor $\sqrt{1 - \frac{M}{N}}$ is applied for the second term, which shows in Equ. (5.7). For both analyses, N=54 and M=142. The fill-to-fill uncertainty for diffractive EM-jet analysis is about 0.3%

$$\sigma^2(P_{fill}) = \sigma^2(P_0) + \sigma^2(\frac{dP}{dt}) \cdot (\frac{\sum_{run} t_{run} L_{run}}{L_{fill}} - t_0)^2 + (\frac{\sigma(fill - to - fill)}{P})^2 \cdot P_{fill}^2 \tag{5.5}$$

$$P_{set}^2 = (\frac{\sum_{run} t_{run} L_{run}}{L_{fill}}) \tag{5.6}$$

$$P^2_{fill-to-fill\,scale} = (1 - \frac{N}{M}) \cdot P^2_{set} \tag{5.7}$$

In summary, the polarization uncertainty is calculated in the quadrature. For the diffractive EM-jet analysis, it's about 3%.

Appendix A

Run list

Appendix B

Trigger distribution

Appendix C

Roman Pot simulation

In Roman Pot simulation, PYTHIA8 generates the particle level events and GEANT4 is used for the RP detector level simulation.

The version of PYTHIA8 used in this analysis is 8.2.35 [17]. This Pythia version allows the simulation on diffractive process, including single diffractive, double diffractive and hard diffraction processes. In this analysis, we use the embedded Pythia in STAR database. The class for the embedded Pythia is "StarPythia8". The proton-proton collisions with $\sqrt{s} = 200$ GeV are simulated. There are totally of 4 million events generated in the simulation. The single diffractive processes are selected to simulate the diffractive processes.

After PYTHIA simulation for particle level, GEANT 4 simulation with RP detector is applied in the detector level simulation. This RP simulation framework called "pp2pp" was developed by STAR Roman Pot group [18]. In this analysis, the 2015 geometry is used, where DX magnet and DX-D0 chamber are implemented specifically for Run 15. The particle level simulation results from PYTHIA 8 are used as the input for RP simulation.

After the simulation on RP, the RP tracks are checked. For the west side RP, figure (C.1) shows the number of silicon planes that the west side RP track hits; and figure (C.2) shows the number of silicon planes that the east side RP track hits. From the plot, if we choose to consider the global tracks which are the tracks hitting 2 RP packages, we should consider the tracks which hit more than 4 planes. Also, the tracks hitting 8 planes are dominant. For the data, therefore, the tracks hitting more than 6 planes will be considered to allow more reasonable statistics.

After that, the cut on RP tracks hitting more than 6 planes is applied when analyzing the simulation data. Figure (C.3) show the only east side RP track θ_x (left plot) and θ_y (right plot), and Figure (C.4) show the only west side RP track θ_x (left plot) and θ_y (right plot). The distributions of either θ_x and θ_y are

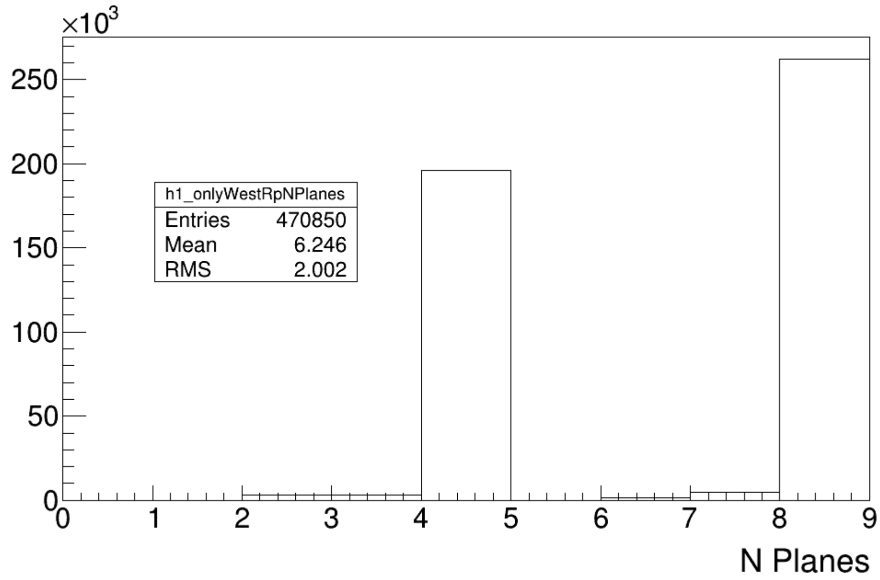

Figure C.1: Number of silicon planes that the west side RP track hits.

similar between the east side and the west side RP tracks. Therefore, the same cuts based on θ_x and θ_y can be considered for both the east side and the west side RP tracks: $-2 < \theta_x < 2$ mrad and $1.5 < |\theta_y| < 4.5$ mrad.

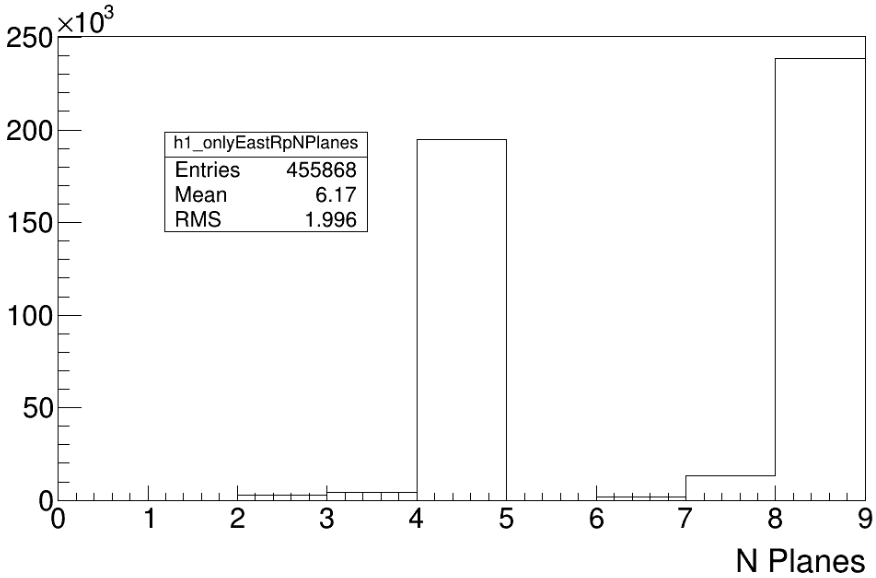

Figure C.2: Number of silicon planes that the east side RP track hits.

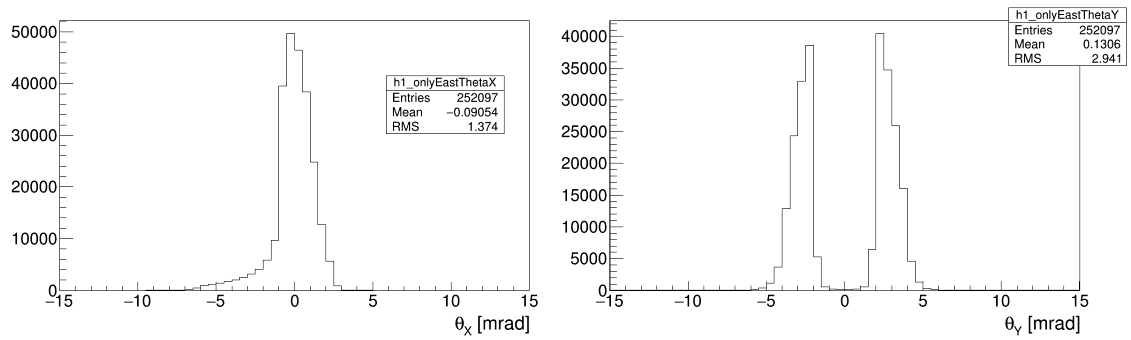

Figure C.3: Distribution of the only east side RP track θ_x (left plot) and θ_y (right plot)

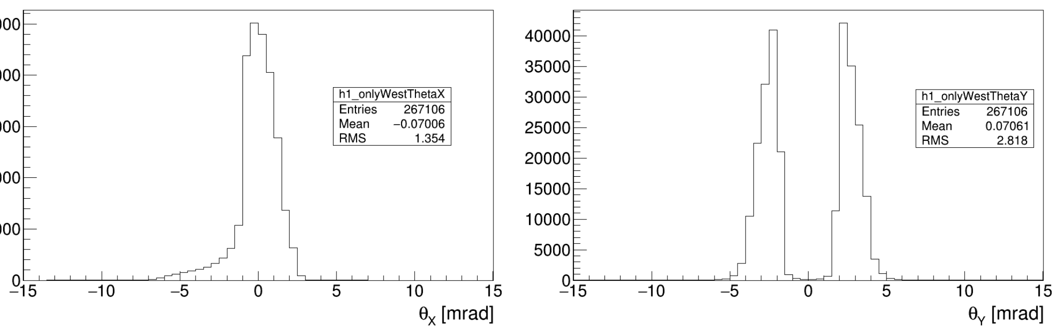

Figure C.4: Distribution of the only west side RP track θ_x (left plot) and θ_y (right plot)

Appendix D

FMS simulation

PYTHIA6 generates the particle level events in the simulation, and GEANT3 is used for the FMS detector level simulation.

For the PYTHIA simulation, the proton-proton collisions with $\sqrt{s} = 200$ GeV are generated, with the tune setting of Perugia6 (Tune parameter 370) [20]. Then, the GEANT3 with FMS detector response implemented under STAR simulation framework ("starsim") are used for the FMS simulation. The Big Full Chain (BFC) proceeds for the event reconstruction. The chain option is "ry2015a agml usexgeom MakeEvent McEvent vfmce Idst BAna l0 l3 Tree logger fmsSim fmspoint evout -dstout IdTruth bigbig fzin geantout clearmem sdt20150417.193427". The EM-jet reconstruction is proceeded along with the BFC process. The Anti-k_T algorithm with R=0.7 is used for the EM-jet reconstruction, the same as the EM-jet reconstruction for data. Details of the EM-jet reconstruction are shown in 2.4. In addition, the event filter (StFmsFilterMaker) and the trigger simulator (StFmsTriggerMaker) are applied during the BFC process. The former filter is based on the energy sum per FMS quadrant, while the latter filter is based on the FMS trigger. Finally, those events passing the filter in the event level and the trigger are saved for both particle level and detector level.

Bibliography

[1] D.L. Adams *et al.*, Phys. Lett. B 261, 201(1991)

[2] B.I. Abelev *et al.* (STAR Collaboration), Phys. Rev. Lett. 101, 222001(2008)

[3] A. Adare *et al.* Phys. Rev. D 90, 012006 (2014)

[4] E.C. Aschenauer *et al.*, arXiv:1602.03922

[5] J. Adam *et al.* (STAR Collaboration), Phys. Rev. D 103, 092009 (2021)

[6] G. L. Kane, J. Pumplin, and W. Repko. Phys. Rev. Lett. 41, 1689 (1978)

[7] D. Sivers, Phys. Rev. D 41, 83 (1990)

[8] J. Collins, Nucl Phys B 396 (1993) 161

[9] J.W. Qiu and G. Sterman, Phys. Rev. Lett. 67 2264 (1991)

[10] M.M. Mondal (STAR Collaboration) PoS (DIS2014) 216

[11] V. Khachatryan *et al.* (CMS Collaboration) Phys. Rev. D 92, 012003 (2015)

[12] Z. Zhu, https://drupal.star.bnl.gov/STAR/system/files/AnalysisNote_0601_0.pdf

[13] M.Cacciari, G. P. Salam, and G. Soyez, Eur. Phys. J. C (2012) 72: 1896

[14] C. Kim, https://drupal.star.bnl.gov/STAR/system/files/fmsCalib_0.pdf

[15] C. Kim, https://drupal.star.bnl.gov/STAR/system/files/note_9.pdf

[16] https://drupal.star.bnl.gov/STAR/blog/oleg/spin-patterns-and-polarization-direction

[17] T. Sjöstrand *et al.*, arXiv:1410.3012

[18] https://drupal.star.bnl.gov/STAR/system/files/LFS_UPC_Geant4SimulationOfRomanPots_17Octobe

[19] B. B. Abelev *et al.* (ALICE Collaboration), Phys. Rev. D 91, 112012 (2015)

[20] P. Skands, arXiv:1005.3457

[21] C. Dilks, https://drupal.star.bnl.gov/STAR/system/files/aLL_analysis_note_1.pdf

[22] Run 15 polarization , https://wiki.bnl.gov/rhicspin/Run_15_polarization

[23] W. B. Schmidke, RHIC polarization for Runs 9-17 , Technical Report BNL-209057-2018- TECH, Brookhaven National Laboratory (2018)